








Exchange-induced spin polarization in a single magnetic molecule junction

Tian Pei^{1,6}, James O. Thomas ^{1,2,6}, Simen Sopp ¹, Ming-Yee Tsang¹, Nicola Dotti¹, Jonathan Baugh ³, Nicholas F. Chilton ⁴, Salvador Cardona-Serra⁵, Alejandro Gaita-Ariño ⁵, Harry L. Anderson ² & Lapo Bogani ¹✉

Many spintronic devices rely on the presence of spin-polarized currents at zero magnetic field. This is often obtained by spin exchange-bias, where an element with long-range magnetic order creates magnetized states and displaces the hysteresis loop. Here we demonstrate that exchange-split spin states are observable and usable in the smallest conceivable unit: a single magnetic molecule. We use a redox-active porphyrin as a transport channel, coordinating a dysprosium-based single-molecule-magnet inside a graphene nanogap. Single-molecule transport in magnetic field reveals the existence of exchange-split channels with different spin-polarizations that depend strongly on the field orientation, and comparison with the diamagnetic isostructural compound and millikelvin torque magnetometry unravels the role of the single-molecule anisotropy and the molecular orientation. These results open a path to using spin-exchange in molecular electronics, and offer a method to quantify the internal spin structure of single molecules in multiple oxidation states.

¹Department of Materials, University of Oxford, 16 Parks Road, Oxford OX1 3PH, UK. ²Department of Chemistry, University of Oxford, Chemistry Research Laboratory, Oxford OX1 3TA, UK. ³Institute for Quantum Computing, University of Waterloo, 200 University Ave., N2L 3G1 Waterloo, ON, Canada.

⁴Department of Chemistry, School of Natural Sciences, University of Manchester, Oxford Road, Manchester M13 9PL, UK. ⁵Instituto de Ciencia Molecular, Universidad de València, 2 C/Catedrático José Beltrán, Paterna, Valencia, Spain. ⁶These authors contributed equally: Tian Pei, James O. Thomas.

✉email: lapo.bogani@materials.ox.ac.uk

Molecular spintronics deals with electronic devices in which the active component is a single magnetic molecule so that electronic transport is controlled by the quantum spin states of just one molecular unit^{1–6}. This approach has mainly focused on the long spin-flip times of single-molecule-magnets (SMMs) but questions about the interactions between flowing electrons and localized spin centers remain unanswered: Can intramolecular spin–spin interactions be used to operate a spintronic device? How can spin-exchange interactions be used to spin-polarize the electron flow?

Although exchange interactions inside nanostructures have been investigated in lateral double-quantum-dots⁷ and carbon nanotubes⁸, the exploitation of intramolecular exchange remains largely uninvestigated in single-molecule electronics. Exchange-bias can shift the zero-field tunneling of SMMs⁹, and magnetic molecules have been used to pin inorganic ferromagnetic layers¹⁰ or to interface with surface states^{11,12}. While exchange interactions lie at the foundation of exchange-bias effects^{13–15}, single-molecule devices are, intrinsically, precluded from using long-range order to achieve exchange-bias. Previous results on phthalocyanine-rare-earth double-decker complexes and carbon nanotubes¹⁶ have shown the possibility of observing nuclear spin states^{17,18} and of reading spin-polarized states through intramolecular exchange¹⁹. However, these observations did not allow two differently polarized transport channels to be resolved, and thus no significant spin polarization of the conduction electrons was achieved. Here we demonstrate that internal spin–spin exchange can be used to achieve >95% spin-polarization, splitting differently polarized conduction channels in single-molecule devices. The concept of the device is the following: intramolecular spin exchange between an anisotropic metal ion and an isotropic conduction channel (Fig. 1a) splits the conduction levels into spin up and down for a given SMM orientation, even in the absence of a magnetic field (Fig. 1b)^{17,19}. When only one

transport channel is present, the intramolecular exchange will lead to an additional peak in the zero-field differential conductance, when plotted as a function of gate potential, V_G (Fig. 1c), due to the spontaneous separation of the transport channel into spin-up and down spin channels of the device.

In weakly-coupled single-molecule junctions, electron transport happens via sequential charging events, and not via a continuous electron flow. Therefore an experimental realization of a single-molecule device exploiting exchange interactions is challenging: electron passage needs to affect only one part of the molecule, while the magnetic state of the other part remains unaffected by the sequential addition/removal of electrons. To this aim, we need to design an SMM with two moieties: one through which sequential transport occurs, and a magnetic one that splits the spin-up and spin-down channels of the former via an exchange interaction, without undergoing oxidation or reduction itself. Another requirement for designing unimolecular devices with highly polarized spin currents is that thermal- and lifetime-broadenings must be lower than the intramolecular exchange. This requirement enforces that our devices must operate in the weakly-coupled transport regime. The often-used bonding to gold leads (usually via thiols) produces molecule-electrode couplings of a few to tens of meV^{1,5,20,21}, higher than the typical intramolecular exchange. Coupling to graphene electrodes via π -stacking interactions^{22,23} is usually well below 1 meV, thus providing access to sufficiently weakly-coupled devices such that exchange-induced effects can be resolved¹⁹.

Results

Molecular design and device fabrication. With these principles in mind, we designed the molecule **MP** (Fig. 2a), which consists of a trivalent rare-earth ion (**M**), coordinated by a redox-active porphyrin (**P**) functionalized with two electron-rich pyrene anchor groups, as an electronically-separate spin center that can couple to the graphene via π -stacking. Porphyrin ligands differ from the more commonly used phthalocyanines in that they allow functionalization at the *meso* positions, which confers stronger electronic coupling with the π -system than β -functionalization and is more effective for controlling aggregation. This molecular design has been shown to be effective for bridging graphene nanogaps²². Sequential electron transport occurs via the π -system of the porphyrin moiety, which can be easily reduced and oxidized, while the redox potentials of the rare-earth are inaccessible within the experimental gate-voltage window^{24,25}. The harsh reaction conditions required to insert the lanthanide cation into the porphyrin are incompatible with the ethynylpyrene anchor groups, so we coordinate the porphyrin before bromination and use Sonogashira coupling to attach the anchor groups (Fig. 2a, synthetic procedure in Supplementary Methods). Isostructural compounds are obtained by using different MCl_3 salts^{26,27}, thus allowing insertion of diamagnetic Y(III) (to give **YP**) and magnetic Dy(III) (to give **DyP**), and comparison of the transport properties in the absence and presence of exchange coupling. The metal ion is coordinated via four nitrogen atoms of the porphyrin, and three oxygens of the Kläui cap²⁸, producing a low-symmetry hepta-coordinate metal center. For **DyP**, the coordination geometry produces a strong magnetic anisotropy and a well-defined direction of the magnetic anisotropy of the spin center²⁶, with the principal magnetization axis along the Dy–Co direction (vide infra). The high anisotropy of the Dy(III) ion leads to an exponential decrease of the spin-flip time on lowering the temperature, T , and single-molecule-magnet behavior: when the magnetic field B is swept, the magnetization of the molecule relaxes slower than the sweeping rate, and single molecules display magnetic hysteresis without requiring any three-dimensional

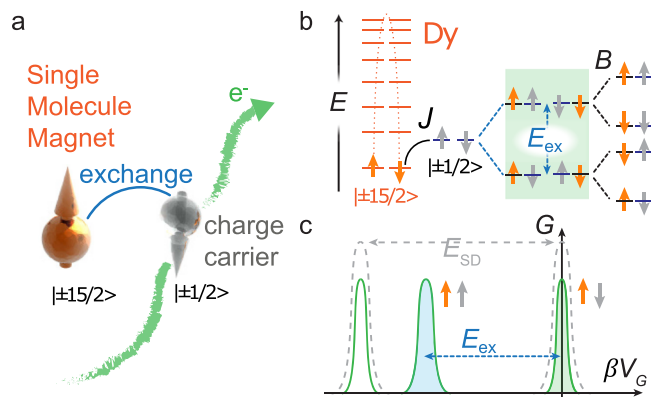


Fig. 1 Exchange-induced polarization in molecular spintronics.

a Intramolecular exchange scheme between the spin of a charge carrier in a localized conduction channel (gray) and a communicating single-molecule magnet (orange). **b** Implementation in **DyP**: the Dy(III) spin center (orange) is subject to an axial magnetic anisotropy and couples to an unpaired electron present on the porphyrin radical cation (gray). The intramolecular exchange coupling J splits the degeneracy of the conduction channel by the exchange energy, E_{ex} , even in zero magnetic fields (green box), application of B field lifts the residual degeneracy. **c** The peaks in the differential conductance vs. gate potential are spaced by the source-drain energy (gray) due to the conduction channel entering and exiting the source-drain window. The exchange induces a splitting of one peak into two spin-polarized channels (blue and green) that are separated by intramolecular exchange energy, E_{ex} , if the gate voltage, V_G , is scaled by the gate lever arm, β . The two channels remain perfectly spin-polarized in $B = 0$ for a slow-relaxing SMM.

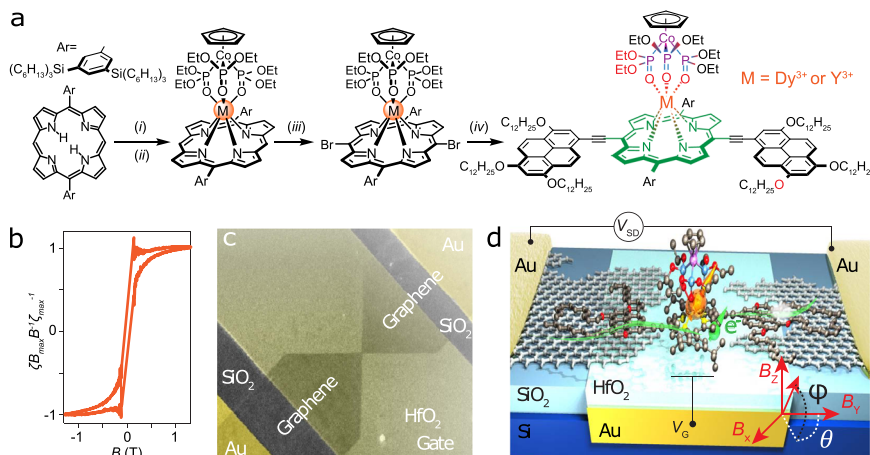


Fig. 2 The molecules and the nanodevices. **a** Scheme of the synthesis of the rare-earth porphyrin molecular complex, **MP**. **M** can be Y³⁺ (no exchange coupling) or Dy³⁺ (introducing the spin exchange). The redox-active porphyrin and the metal center are highlighted in green and orange, respectively. Reagents and conditions: (i) MCl₃·6H₂O, imidazole, benzamidazole, Ph₂O, 200 °C, 16 h; (ii) Na[CpCo{P(O)(OEt)₂}]₃, (iii) N-bromosuccinimide, CH₂Cl₂; (iv) 1,3,6-tris(dodecyloxy)-8-ethynylpyrene, Pd(PPh₃)₄, CuI, DIPA, 65 °C, 16 h. **b** Hysteresis cycle detected by cantilever-torque magnetometry at 150 mK with a field-sweep rate of 0.125 T/min, showing single-molecule-magnet behavior for **DyP** derivative. The torque signal ζ is divided by the applied magnetic field B and normalized by the high-field signal $\zeta_{\text{max}}/B_{\text{max}}$. **c** False-color SEM image of the devices, showing Au pads (yellow), the Au/HfO₂ back-gate (gray), and the graphene electrodes (darker shade). **d** Scheme of the experiment on **DyP** and the reference frame of the magnetic field B (red). The Dy(III) spin center (the orange) sits on the redox-active porphyrin, which spans the nanogap and exchanges electrons (green) via pyrene anchor groups.

ordering^{2,5,9,26,27}. This hysteresis is indeed observed at temperatures comparable to the transport experiments using a torque magnetometer (Fig. 2b) and the full angular dependence of the anisotropy, as a function of the orientation of the magnetic field can be extracted (detailed in Methods section).

Fabrication of the devices follows a published procedure²² that is described in the Methods section. In brief, graphene ribbons are patterned lithographically into a bowtie shape and feedback-controlled electro-burning forms graphene nanogaps that are 1–2 nm, as estimated from the tunneling currents (Fig. 2c)²⁹. Single-molecule transistors are then produced by drop-casting a solution of **MP** in toluene (2 μ M) onto the nanogaps. A local gate electrode, separated by 10 nm of HfO₂, runs under the tunnel junction allowing the molecular levels to shift with respect to the chemical potential of the leads by a gate voltage V_G (Fig. 2c, d) and modulating the current I_{SD} produced by the source-drain voltage V_{SD} .

Charge transport measurements. Figure 3a, b and Supplementary Fig. 26 show the stability diagrams of the differential conductance $G_{SD} = \partial I_{SD} / \partial V_{SD}$ vs. V_{SD} and V_G for several **MP** devices. The observation of Coulomb blockade confirms that graphene-**MP** molecular devices operate in the desired weakly-coupled transport regime, with $\Delta E \gg k_B T, \Gamma$, where ΔE is the energy spacing between molecular levels, k_B is the Boltzmann constant and $\Gamma = \Gamma_S + \Gamma_D$ is the electronic coupling to the source and drain electrodes^{24,30}. For weakly-coupled molecular junctions, single-electron tunneling is the mechanism of charge transport, with regions of blocked current produced by Coulomb repulsion where the charge on the molecule is fixed. Between these regions, current flows through the weakly-coupled molecular junction as a result of sequential electron transfer to (i.e., a reduction process) and from (i.e., an oxidation process) the molecule. Within sequential tunneling regions, several lines of higher conductance are visible, running parallel to the diamond edges or slanted: parallel lines are molecular states, while slanted lines correspond to interference inside graphene leads, unrelated to molecular behavior³¹. Our measurement conditions impose that $\Delta E > \Gamma, k_B T$, so that Γ can be determined³² as the full-width

half-maximum of G_{SD} vs. V_G at $V_{SD} = 0$ mV (Supplementary Fig. 27). For the **YP** and **DyP** devices presented in Fig. 3 we obtain $\Gamma = 0.30$ meV (**YP**) and 0.34 meV (**DyP**). As $k_B T \sim 2 \mu$ eV at 20 mK, this indicates lifetime broadening due to Γ , rather than thermal broadening, is the main contribution to the signal broadening. The electrostatic coupling between the gate potential and the molecular states is given by the gate lever arm, β , (0.23 for **YP** and 0.085 for **DyP**, Supplementary Fig. 27) and this allows us to convert between V_G and the intrinsic energy scales of the molecule. The variation in β is attributed to imperfections in the gate dielectric or different screening of the gate-field by the source and drain electrodes and is in-line with previous reports on graphene single-molecule devices^{22,33}.

By choosing V_G , the molecule can be fixed in the **MP**, **MP**⁺, or **MP**⁻ oxidation state, (see Supplementary Discussion and Supplementary Fig. 28 for details of the assignment) due to Coulomb blockade^{24,34}. The transport regions that are studied in detail (Fig. 3a, b) are the **MP**⁺/**MP** transitions. The creation of **MP**⁺ by removing an electron from the redox-active porphyrin leads to a state that contains, in addition to the M(III) center, a spin-1/2 radical delocalized inside the porphyrin π -system. We first investigate the molecular system without exchange interactions, **YP**. A magnetic field B splits the **YP**⁺ transition into two diverging states, corresponding to the spin-up and spin-down states of the electrons flowing through the porphyrin channel (Fig. 4a). The states are separated by $\Delta E = g\mu_B B = \beta\Delta V_G$, where μ_B is the Bohr magneton, and g is the Landé factor of the $s = 1/2$ porphyrin radical in the **YP**⁺ state. As expected for a Kramers doublet, no splitting is present at $B = 0$ and the fitted $g = 1.7 \pm 0.2$ matches that expected for an electron spin in a porphyrin ring ($g \sim 2$)³⁴ (Fig. 4e, gray points).

In **DyP**, where the intramolecular exchange is introduced, a new molecular state appears at 0.8 ± 0.1 meV above **DyP**⁺/**DyP** (Fig. 3b). The excited state meets the Coulomb diamond edge on the **DyP**⁺ side, indicating that this is an excitation of the cationic state **DyP**⁺, rather than of **DyP**, and we shall thus call it **DyP**⁺*. The evolution of the **DyP**⁺/**DyP** and **DyP**⁺*/**DyP** transitions, as a function of the magnitude and direction of B , are very rich (Fig. 4b–d). The behavior perpendicular to the plane of the graphene, B_z , is strongly nonlinear, with a pronounced and

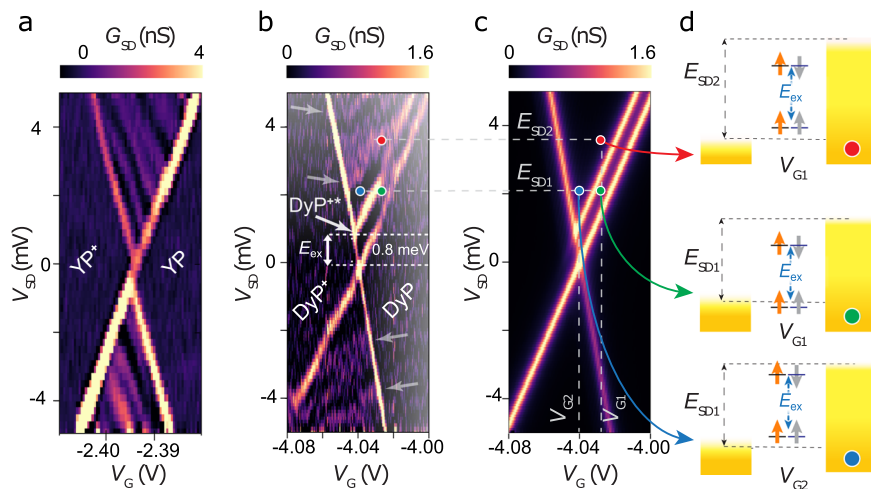


Fig. 3 Single-molecule transport measurements. **a** Map of the differential conductance $G_{SD} = \partial I_{SD} / \partial V_{SD}$, vs. V_G and V_{SD} for **YP**, at 20 mK, at $B = 0$. Coulomb diamonds are labeled with molecular states. **b** G_{SD} map of the **DyP⁺/DyP** transition at $B = 0$ and 20 mK. Gray arrows indicate interference from graphene leads. The excited spin state, **DyP⁺*** is visible (white arrow) and marks indicate representative transport regions. **c** Simulation of the differential conductance map for the **DyP⁺/DyP** transition. Marks indicate representative transport regions. **d** Transport channels are available in the different regions, with the molecular energy levels depicted between the electrode energies (yellow). Arrows indicate the ferro- and antiferromagnetic arrangements of the Dy (orange) and flowing electron spin (gray).

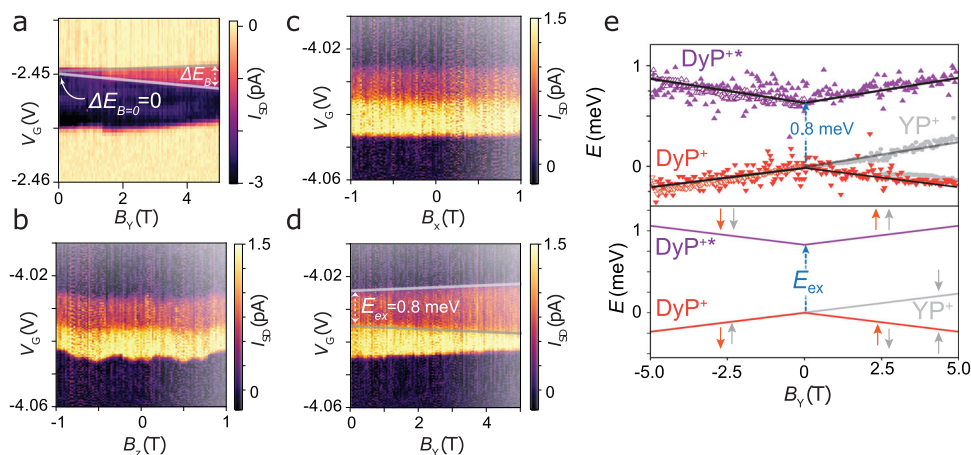


Fig. 4 Exchange splitting. **a** Splitting of the lowest energy peak for the **YP** device, on increasing B_Y , acquired at $V_{SD} = -1.5$ mV. A spin doublet is visible (gray lines), without exchange. **b** Dependence of the ground state and excited state transition potentials for **DyP⁺/DyP** on increasing B_Z , acquired at $V_{SD} = 1.5$ mV. **c** Dependence of ground state and excited state transition potentials for **DyP⁺/DyP** on increasing B_X , acquired at $V_{SD} = 1.5$ mV. **d** Dependence of ground state and excited state transition potentials for **DyP⁺/DyP** on increasing B_Y , acquired at $V_{SD} = 1.5$ mV. **e** Upper panel shows a separation of the magnetic levels vs. B_Y , for two **DyP** devices (triangles, full and open) and for the **YP** device (gray circles). Lines are fits to the data. Lower panel, expected evolution of the magnetic field levels for **DyP⁺** (color) and **YP⁺** (gray). Dy(III) spins are orange and porphyrin ones gray. All data were acquired at 20 mK.

symmetrical displacement about $B_Z = 0$. In contrast, along B_X the transitions remain largely independent of field strength in the range $-1 \text{ T} < B_X < 1 \text{ T}$. We attribute this to the rough alignment of the molecular easy axis normal to the graphene plane (vide infra for a more detailed discussion of the anisotropy). The two **DyP⁺*** and **DyP⁺** levels clearly diverge vs. increasing $|B_Y|$, indicating that they must have different spin states (Fig. 4d).

Figure 4e shows the B_Y -dependence of the energies of the **DyP⁺** and **DyP⁺*** transitions, for both positive and negative B_Y , for different **DyP** devices, and compared to that of **YP**. The electronic transport and the spin splitting are reproducibly observed in different devices and among different chips and is consistent whatever the sign of B_Y . The slope of the divergence is consistent with the **YP** data, and electronic Landé g factors of 1.7 ± 0.4 and 1.9 ± 0.2 are measured for two **DyP** devices,

compatible with the sensing of the electron spin localized on the porphyrin moiety. The 0.8 meV level splitting in $B_Y = 0$, which is visible only for **DyP** devices, cannot arise from electric field effects or transverse anisotropy terms: Kramers parity theorem strictly forbids any zero-field-splitting for both the unpaired porphyrin spin and the Dy(III) ion. On the contrary, the splitting is a fingerprint of the intramolecular exchange interaction, as outlined in the following paragraph.

For **DyP⁺** the porphyrin spin $s = 1/2$ is roughly-isotropic, while Dy(III) is a highly anisotropic ${}^6\text{H}_{15/2}$ center, with a spin-orbit-coupled angular momentum $J = 15/2$. The spin Hamiltonian of the system is thus:

$$\hat{H} = \hat{s}\hat{J} + \hat{s}\hat{D}\hat{J} + \mu_B \hat{B}\hat{G}\hat{J} + \mu_B \hat{B}\hat{g}\hat{s} + \sum_{k=2,4,6} \sum_{q=-k}^k B_{kq} \hat{O}_k^q \quad (1)$$

where \mathbf{J} is the exchange interaction tensor, \mathbf{D} the dipolar spin–spin coupling tensor, \mathbf{G} and \mathbf{g} are the Landé tensors for Dy and the porphyrin, respectively, and the sum contains Stevens operator equivalents, i.e., a sum with weights B_j over the tesseral harmonics operators O_j . The Stevens operators, because of the high value of B_{20} in Dy systems, split Dy(III) spin levels into a series of different Kramers doublets even at zero-field (Fig. 1b). At $T < 5$ K we can consider only the lowest-lying Kramer’s doublet and Dy(III) behaves as an effective spin $S_{\text{eff}} = \frac{1}{2}$ with a large effective Landé factor $G_{\text{eff}} \sim 18$ ²⁶. We can therefore identify the different transitions observed in the experimental data to different spin states of DyP^+ using the assignment: $|m_s, m_{S_{\text{eff}}}\rangle$. The ground state DyP^+/DyP transition (occurring at zero bias voltage) is via the antiferromagnetic $| -1/2, 1/2 \rangle$ and $| 1/2, -1/2 \rangle$ state of DyP^+ (hereafter indicated with $\uparrow\downarrow$). The excited state $\text{DyP}^{*+}/\text{DyP}$ transition at 0.8 ± 0.1 meV above the ground state transition is via the ferromagnetic ($\uparrow\uparrow$) $| 1/2, 1/2 \rangle$, $| -1/2, -1/2 \rangle$ state of the cation, with the energy splitting corresponding to the exchange energy, E_{ex} . Excellent agreement is obtained between the resulting energy vs. B_Y evolution and the experimental data, for an antiferromagnetic exchange interaction, between S_{eff} and s , $J = -2$ $E_{\text{ex}} = -1.6 \pm 0.2$ meV (Fig. 4e). The YP system is much simpler by design. The electron configuration of Y(III) is closed-shell [Kr], so there are no unpaired spins or unquenched orbital angular momentum ($S = 0$, $L = 0$), and hence it functions as a control molecule because no intramolecular exchange interactions are present. The relevant spin states are solely due to the unpaired spin on the porphyrin of YP^+ , $|m_s\rangle = |\pm 1/2\rangle$, and the only spin Hamiltonian term that remains accounts for Zeeman splitting of these ($\hat{H} = \mu_B \hat{B} \hat{g} \hat{s}$). This expected behavior is observed in the experimental data (Fig. 4a, e).

A master-equation framework (outlined in Supplementary Discussion)³⁵ allows the full stability diagram to be calculated, again in excellent agreement with the data of Fig. 3b (see Fig. 3c). Different conductance regions correspond to different states involved in the current (Fig. 3d). For a fixed orientation of Dy(III), two energy levels of DyP^+ , with a different spin on the porphyrin ring can both contribute to transport if the bias window is sufficiently large (top, red marker) or if the gate voltage is sufficiently negative (bottom, blue marker). Conversely, there is a region where transport occurs via one state of DyP^+ , corresponding to the antiferromagnetic spin configuration $\text{DyP}^+_{\uparrow\downarrow}$ (middle, green marker). In this region only the electrons with the same spin as Dy(III) can tunnel from the HOMO of DyP to generate $\text{DyP}^+_{\uparrow\downarrow}$, and only electrons of that same spin can tunnel into the SOMO of $\text{DyP}^+_{\uparrow\downarrow}$, owing to Pauli exclusion. In this way the device allows the passage solely of conduction electrons with the same spin as Dy(III). The magnetometry data (Fig. 2b) confirms that at low or zero magnetic field, S_{eff} can be fixed, and as a consequence the molecule can act as a spin-polarizer. A small magnetic field initializes S to either orientation depending on the field-direction, and the intramolecular exchange splitting gives rise to a spin-polarized current of either $m_s = \frac{1}{2}$ or $m_s = -\frac{1}{2}$. The splitting of the conductance peak is clearly observable in its gate dependence for YP^+ and DyP^+ (Fig. 5a): the exchange splitting leads to the creation of an additional conductance peak in perfect agreement with the predictions of Fig. 1c. We can fit the conductance peaks to extract the separate contributions ($I_{\uparrow\downarrow}$ and $I_{\uparrow\uparrow}$) that occur via the different states of DyP^+ to I_{SD} (Fig. 5b) (see Methods for the fitting procedure). As the intramolecular exchange interaction is large compared with the lifetime and thermal broadening the resulting current polarization ratio $P = (I_{\uparrow\downarrow} - I_{\uparrow\uparrow}) / (I_{\uparrow\downarrow} + I_{\uparrow\uparrow})$ is very high, and reaches 0.94 ± 0.35 for a V_G region of 5.4 mV even at $B = 0$. Due to the additional splitting

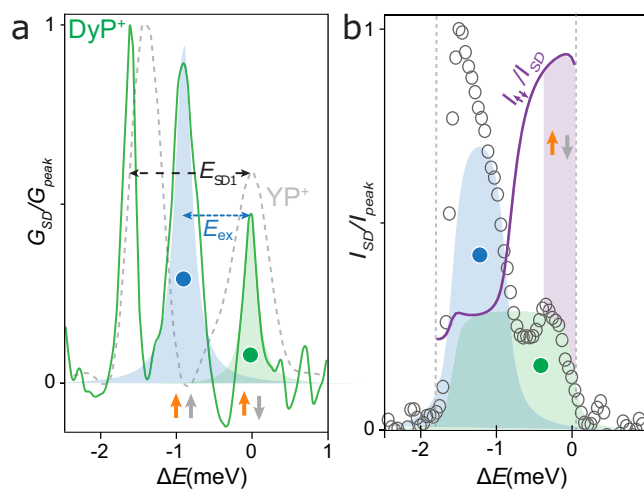


Fig. 5 Molecular polarization effect. **a** Zero-field conductance of YP^+ (gray) and DyP^+ (green) devices at $E_{\text{SD}} = 1.5$ mV vs. the energy displacement [$\Delta E = \beta_{\text{MP}} (V_G - V_C)$, where V_C is the gate voltage of the Coulomb peak]. The splitting of the conductance peak induced by the exchange is highlighted in blue. Curves are scaled for their maximum peak value, for clarity. Shaded areas are Lorentzian fits, and marks indicate the conduction mechanism as in Fig. 3, panel d. **b** Contributions to the current of DyP^+ (gray circles) by the ferromagnetic (blue) and antiferromagnetic (green) molecular transport channels. Curves are scaled for their maximum peak value to compare to the fraction of spin-polarized electrons (violet). The violet region indicates a polarization higher than 90%, colored marks indicate the conduction mechanisms, as in Fig. 3.

of the peaks as a result of the Zeeman effect this region increases further in size to 8 mV with $B_Y = 5$ T (Supplementary Fig. 30) with a maximum of $P = 0.97 \pm 0.28$.

Magnetic anisotropy. As exchange interactions are dependent on the mutual orientation of the spins, and can be extremely sensitive to the large anisotropy of rare-earth, they also offer a way to probe the orientation of the molecular easy axis via single-molecule experiments. The single-ion anisotropy will produce fingerprints in the magnetoconductance signal and modulate it as a function of the orientation of the magnetic field. We carried out a complete characterization of the DyP^+ and DyP^{*+} levels vs. the angles of B , in the plane of the graphene, θ , and out-of-plane, φ (Fig. 6a, b). No appreciable angular dependence is observed for θ , on the contrary, a non-monotonous angular dependence is observed for φ , with DyP^{*+} displaying several local energy minima and maxima, with a periodic pattern (Fig. 6b). These observations, in combination with the variation with field strength (Fig. 3), lead to the conclusion that the axial anisotropy of the Dy(III) is roughly lying along the laboratory frame z -axis, perpendicular to the graphene plane. Calculation of the magnetic anisotropy of the molecular system with ab initio methods (see Methods) reveals that the magnetic anisotropy of the Dy(III) center is tilted to the plane of the porphyrin at an angle of ca. 70° (Fig. 6b and Supplementary Fig. 31). A much less structured angular evolution is expected when rotating B in the porphyrin plane along θ , owing to the axial anisotropy of the lowest Kramers doublet (Supplementary Table 1).

The angular dependence can be described, without loss of generality, as the sum: $E = \sum_n C_n \cos(2n\varphi)$, where the C_n indicate the weights of the cosine terms (values in Supplementary Table 2), and the resulting fits in Fig. 6c show energy minima that indicate a tilted magnetic easy cone anisotropy of Dy(III) at a tilt angle of

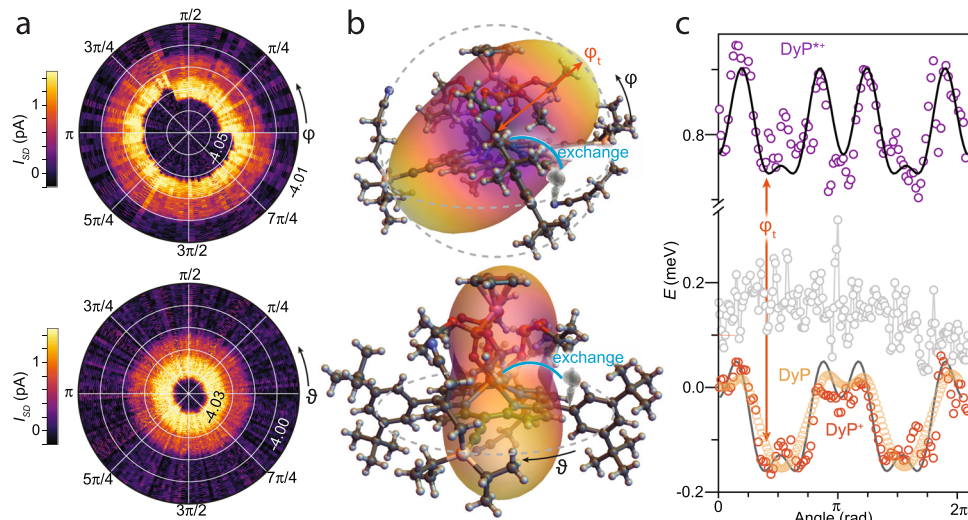


Fig. 6 Angular relation to single-ion anisotropy. **a** Measured angular evolution of the exchange effect, showing the current (color scale) vs. V_G (radial) and the angle (top: out-of-plane φ ; bottom: in-plane θ), under constant magnetic field-magnitude $|B| = 1$ T, at $V_{SD} = 1.5$ mV. A charge jump is observed for $0 < \varphi < 2\pi/3$. **b** Iso-energy representation of the single-ion anisotropy of the Dy(III) ion, superimposed onto the molecular structure, as viewed from sideways in the single-molecule device architecture (top) and along the electron transport channel (bottom). **c** Angular evolution of the energy, relative to the ground state at zero angle, of the DyP^{2+} (violet) and DyP^{+} (orange) states vs. φ , with the anisotropy energy extracted from torque measurements on the DyP at the same temperature superimposed (yellow). The lack of evolution vs. θ is also shown (gray). Black lines are fits to the data (see text). All data were acquired at 20 mK.

$\varphi_t = 68^\circ$. The correspondence of the tilt angle of the Dy(III) anisotropy measured within the lab frame and the ab initio calculated values within the porphyrin framework indicates the porphyrin plane is sitting roughly on the surface, which indeed is what is expected from the molecular design. Both the DyP^{+} and DyP^{2+} levels display the same overall symmetry, as expected because they both arise from the exchange of Dy(III) with an unpaired electron on the porphyrin ring, but DyP^{2+} displays much more pronounced energy oscillations at $\varphi = 0, \pi$, in agreement with an antiferromagnetic interaction.

We can now directly compare the single-molecule transport with angular-resolved CTM measurements on the neutral DyP system, performed in the same conditions at mK temperatures. The anisotropy energy that is extracted from torque measurements via the relation $\zeta_z = \delta E(\phi)/\delta \phi$ shows the presence of the same anisotropy signal in the φ dependence (Fig. 6c), with the difference that the neutral system lacks the unpaired spin in the porphyrin, as revealed by the signal around $\varphi = \pi/2$. By comparing the behavior of the single-molecule device and crystals, we can thus demonstrate that the single-ion anisotropy influences the magneto-resistive signal of transport electrons via the exchange interaction, and will modulate the transport characteristics of molecular spintronic devices.

Discussion

These results demonstrate that the spin exchange internal to a molecule can be used to control the electron flow through it, and obtain high spin polarization in the tunneling current. The angular dependence provides a direct insight into the role of the molecular anisotropy on the modulation of the transport. Before any optimization, the resulting spin polarization, $94 \pm 35\%$, already outclasses many bulks and single-molecule spin polarizers^{36,37}. We use gate and field-dependent measurements at low temperatures to show how the interplay between the molecule-electrode coupling strength and the intramolecular exchange energy is crucial to obtain this high degree of polarization. The relevant internal energy scale, J , can

reach up to hundreds of K in molecular magnets, so that polarization is conceivable at temperatures well above those used in this demonstration, especially when using graphene electrodes²⁹. Our observations have several implications regarding the utility of such a highly polarized tunneling current. The possibility of hybrid devices can be explored, integrating spin detectors directly onto the graphene³⁸ but far from the junction, to investigate the dependence of the μm long spin coherence length of graphene on the tunnel barriers and the presence of other magnetic molecules. Alternatively, modular porphyrin chemistry can be used to integrate a second porphyrin directly into the molecular structure²⁶, such that the spin-polarized current injected into the first porphyrin can be read out by the second, creating a molecular spin valve. Integration of all the elements of a spintronic device in a single molecule, thus avoiding magnetic electrodes, is a desirable goal. The fundamental demonstration from this study that a lanthanide porphyrin acts as a highly effective spin-polarizer, is a key first step to create such a device. Furthermore, these results open completely new perspectives for the investigation of magnetic molecules, offering a new methodology to unravel the internal interaction patterns, even for different oxidation states and in non-crystalline environments.

Methods

Device fabrication. An array of local gate electrodes (Ti/Au, 40 nm thick) was patterned onto a doped Si/SiO₂ substrate via photolithography. Second, a 10 nm layer of HfO₂ was deposited by atomic layer deposition (ALD) to isolate the gate electrode. Then pairs of Ti/Au source and drain electrodes (60 nm thick) were added via a second photolithography step on top of the ALD layer. CVD-grown graphene was transferred onto the substrate using wet-transfer techniques and was etched into bowtie shapes using electron-beam-lithography and O₂-plasma etching. A gap was opened in the graphene constriction using feedback-controlled electroburning in air and I - V characteristics were recorded for every device³⁹. 2 μL of solutions of MP were drop-cast onto the nanogaps and the devices dried and measured.

Determination of transport parameters. The transport measurements were performed in an OI-Triton dilution refrigerator using low-noise DC electronics

(Delft- and home-made). The refrigerator is equipped with a vector magnet that can apply up to 1/6 T along the $B_x/B_y/B_z$ axes. The electron temperature measured after the powder filtering is ~ 25 mK, corresponding to $k_B T \sim 2$ μ eV. The energies of the different molecular states were extracted from the transport data presented in Fig. 4 (field strength) and Fig. 6 (field angle) by the following procedure. Firstly, the $I_{SD}-V_G$ measurement taken at each B -field was differentiated with respect to V_G . A Lorentzian function was fitted to each peak in the dI_{SD}/dV_G vs. V_G , and the centers of the Lorentzian are assigned to the potentials of the transitions. The potentials (in V_G) are then converted into energies by multiplication by the gate lever arm, β . Thereby we can extract the energies of the $DyP_{\uparrow\downarrow}^+ / DyP$, and $DyP_{\uparrow\uparrow}^+ / DyP$ transitions. Simple subtraction of the energy of the ground state at $B = 0$ or at an angle of 0 yields the relative energies of $DyP_{\uparrow\downarrow}^+$ and $DyP_{\uparrow\uparrow}^+$ that is plotted as a function of B_y (Fig. 4) and field angles (Fig. 6). The parameters extracted from the fits to the E vs. B_y (e.g., g -factors) are reported in the main text with errors of ± 2 standard deviations. The standard deviation is calculated from the variance returned from the fitting procedure. The fits of the non-linear data in Fig. 6 are accompanied by standard errors of regression. A full list of the parameters of these fits is given in Supplementary Table 2. The method for estimating the current through AFM and FM channels is outlined in detail in the Supplementary Discussion.

Cantilever-torque magnetometry. Cantilever-torque magnetometry (CTM) measures the magnetic torque that arises when a magnetic sample is placed in a homogeneous magnetic field, B . When B is applied in a different direction than the magnetization M there is a magnetic torque: $\zeta = M \times B$. The torque is a result of the energy dependence of the system as a function of the angle ε between M and B , $\zeta = -\partial E / \partial \varepsilon$. It can be shown that ζ can be expressed through orthogonal (x, y, z) components:⁴⁰

$$\zeta_y = B^2 (M_x/B_x - M_z/B_z) \sin \varepsilon \cos \varepsilon \quad (2)$$

This result implies that $\zeta_y \neq 0$ only if $M_x/B_x - M_z/B_z = \chi_{xx} - \chi_{zz} \neq 0$, i.e., if the system is magnetically anisotropic (χ is the magnetic susceptibility tensor). We note that ζ is a direct manifestation of the magnetic anisotropy in the sample and is insensitive to isotropic contributions to M .

CTM exploits magnetic torque by mounting a single-crystalline sample on a metallic cantilever before applying a magnetic field (see Supplementary Fig. 23 for device structure). Single crystals of **DyP** could not be obtained, due to the four trihexylsilyl groups and six dodecyl chains that decorate the structure (required for conferring solubility and increasing non-covalent interactions with the graphene electrodes respectively). Therefore CTM was carried out on **DyP'** (see Supplementary Fig. 23 for chemical structure) which retains the ligand-field environment of **DyP** but has substitutions to the molecular periphery to promote crystallization²⁶. The direction of magnetization of the sample is pinned by anisotropy along a favorable crystallographic direction, and torque is generated by the misalignment ε of the sample magnetization and applied field orientations. The torque bends the thin cantilever to reduce ε . In our setup the cantilever is separated from an underlying parallel metal plate by vacuum at a distance d . The small torque-induced deflections of the cantilever can be detected by measuring the capacitance between the cantilever and plate: $C \propto 1/d$. Finally, it can be shown that, $\zeta(B) = C_0/C(B) - 1$, where $C_0 = C(B = 0)$, which gives the qualitative ζ -versus- B behavior⁴⁰.

We used CTM to assess qualitatively the magnetic anisotropy of the sample by measuring the torque response upon rotating B (with a fixed magnitude of 0.9 T) in the xz plane, as illustrated in Supplementary Fig. 23. The observed torque is a direct manifestation of magnetic anisotropy in this plane, and reveals information about “easy” and “hard” magnetic directions, which can be identified in the lab frame as $\phi(\zeta = 0)$ ⁴¹. Furthermore, we have measured ζ_y as a function of B with fixed $\phi = -50^\circ$ and changing magnitude in order to detect magnetic hysteresis. From Eq. 2, $M \propto \zeta_y/B$, i.e., the anisotropic part of M in the chosen plane is given by ζ_y/B . After several field-sweep cycles the ζ_y signal was averaged to yield the magnetic field curves as shown in Fig. 2b (main text). Note that because ζ vanishes at $B = 0$ the calculation of ζ_y/B produces diverging values at fields close to zero. As a consequence, the signal close to $B = 0$ has been replaced by straight lines due to the vanishing zero-field torque signal. In our hysteresis measurements, we also observe instrumental noise around zero-field that adds to this effect.

Ab initio calculations. In order to estimate the magnetic anisotropy in the **DyP** molecule, we have performed ab initio complete active space self-consistent field spin-orbit (CASSCF-SO) calculations with OpenMolcas⁴². We have used the geometry from X-ray crystallography without optimization and used basis sets from the ANO-RCC library^{43–46} with VTZP quality for Dy, VDZP quality for the atoms in the first coordination sphere, and VDZ quality for all other atoms. Two-electron integrals were decomposed using the Cholesky method with a 10^{-8} threshold to save resources. Relativistic effects were treated using the second-order Douglas–Kroll–Hess transformation where scalar contributions were taken into account at the spin-free level, and the spin-orbit coupling was applied in a state-

interaction framework. The active space consisted of nine electrons in the seven 4f orbitals of Dy(III), and we performed state-average CASSCF calculations for 18 sextets accounting for the lowest-lying 6H and 6F terms. Then, all 18 sextets were mixed by spin-orbit coupling to yield the final eigenstates (Supplementary Table 1).

Data availability

The datasets generated during and/or analyzed during the current study are included in this published paper (and its supplementary information files) or available from the corresponding author on request.

Received: 4 November 2020; Accepted: 8 July 2022;

Published online: 03 August 2022

References

- Aradhya, S. V. & Venkataraman, L. Single-molecule junctions beyond electronic transport. *Nat. Nanotechnol.* **8**, 399 (2013).
- Bogani, L. & Wernsdorfer, W. Molecular spintronics using single-molecule magnets. *Nat. Mater.* **7**, 179–186 (2008).
- Heersche, H. B. et al. Electron transport through single Mn₁₂ molecular magnets. *Phys. Rev. Lett.* **96**, 206801 (2006).
- Park, J. et al. Coulomb blockade and the Kondo effect in single-atom transistors. *Nature* **417**, 722–725 (2002).
- Burzuri, E., Zyazin, A. S., Cornia, A. & van der Zant, H. S. J. Direct observation of magnetic anisotropy in an individual Fe₄ single-molecule magnet. *Phys. Rev. Lett.* **109**, 147203 (2012).
- Jo, M.-H. et al. Signatures of molecular magnetism in single-molecule transport spectroscopy. *Nano Lett.* **6**, 2014–2020 (2006).
- Hanson, R. et al. Spins in few-electron quantum dots. *Rev. Mod. Phys.* **79**, 1217–1265 (2007).
- Laird, E. A. et al. Quantum transport in carbon nanotubes. *Rev. Mod. Phys.* **87**, 703–764 (2015).
- Wernsdorfer, W., Aliaga-Alcalde, N., Hendrickson, D. N. & Christou, G. Exchange-biased quantum tunnelling in a supramolecular dimer of single-molecule magnets. *Nature* **416**, 406–409 (2002).
- Gruber, M. et al. Exchange bias and room-temperature magnetic order in molecular layers. *Nat. Mater.* **14**, 981–984 (2015).
- Lodi Rizzini, A. et al. Coupling single molecule magnets to ferromagnetic substrates. *Phys. Rev. Lett.* **107**, 177205 (2011).
- Nistor, C. et al. Exchange bias of TbPc₂ molecular magnets on antiferromagnetic FeMn and ferromagnetic Fe films. *Phys. Rev. B* **92**, 184402 (2015).
- Meiklejohn, W. H. & Bean, C. P. New magnetic anisotropy. *Phys. Rev.* **102**, 1413–1414 (1956).
- Parkin, S. S. P. et al. Exchange-biased magnetic tunnel junctions and application to nonvolatile magnetic random access memory. *J. Appl. Phys.* **85**, 5828–5833 (1999).
- Nogués, J. & Schuller, I. K. Exchange bias. *J. Magn. Magn. Mater.* **192**, 203–232 (1999).
- Urdampilleta, M. et al. Supramolecular spin valves. *Nat. Mater.* **10**, 502–506 (2011).
- Thiele, S. et al. Electrically driven nuclear spin resonance in single-molecule magnets. *Science* **344**, 1135 (2014).
- Vincent, R. et al. Electronic read-out of a single nuclear spin using a molecular spin transistor. *Nature* **488**, 357–360 (2012).
- Godfrin, C. et al. Electrical read-out of a single spin using an exchange-coupled quantum dot. *ACS Nano* **11**, 3984–3989 (2017).
- Yu, L. H. & Natelson, D. The Kondo effect in C60 single-molecule transistors. *Nano Lett.* **4**, 79–83 (2004).
- Burzuri, E. et al. Franck–Condon blockade in a single-molecule transistor. *Nano Lett.* **14**, 3191–3196 (2014).
- Limburg, B. et al. Anchor groups for graphene-porphyrin single-molecule transistors. *Adv. Funct. Mater.* **28**, 1803629 (2018).
- Thomas, J. O. et al. Understanding resonant charge transport through weakly coupled single-molecule junctions. *Nat. Commun.* **10**, 4628 (2019).
- Perrin, M. L., Burzuri, E. & van der Zant, H. S. J. Single-molecule transistors. *Chem. Soc. Rev.* **44**, 902–919 (2015).
- Bratsch, S. G. Standard electrode potentials and temperature coefficients in water at 298.15 K. *J. Phys. Chem. Ref. Data* **18**, 1–21 (1989).
- Le Roy, J. J. et al. Tailored homo- and hetero-lanthanide porphyrin dimers: a synthetic strategy for integrating multiple spintronic functionalities into a single molecule. *Chem. Sci.* **9**, 8474–8481 (2018).

27. Gao, F. et al. Syntheses, structures, and magnetic properties of seven-coordinate lanthanide porphyrinate or phthalocyaninate complexes with Kläui's tripodal ligand. *Inorg. Chem.* **52**, 6407–6416 (2013).
28. Kläui, W. The coordination chemistry and organometallic chemistry of tridentate oxygen ligands with π -donor properties. *Angew. Chem., Int. Ed. Engl.* **29**, 627–637 (1990).
29. Prins, F. et al. Room-temperature gating of molecular junctions using few-layer graphene nanogap electrodes. *Nano Lett.* **11**, 4607–4611 (2011).
30. Osorio, E. A. et al. Single-molecule transport in three-terminal devices. *J. Phys. Condens. Matter* **20**, 374121 (2008).
31. Gehring, P. et al. Distinguishing lead and molecule states in graphene-based single-electron transistors. *ACS Nano* **11**, 5325–5331 (2017).
32. Beenakker, C. W. J. Theory of Coulomb-blockade oscillations in the conductance of a quantum dot. *Phys. Rev. B* **44**, 1646–1656 (1991).
33. Mol, J. A. et al. Graphene-porphyrin single-molecule transistors. *Nanoscale* **7**, 13181–13185 (2015).
34. Limburg, B. et al. Charge-state assignment of nanoscale single-electron transistors from their current–voltage characteristics. *Nanoscale* **11**, 14820–14827 (2019).
35. Sowa, J. K., Mol, J. A., Briggs, G. A. D. & Gauger, E. M. Beyond Marcus theory and the Landauer–Büttiker approach in molecular junctions: a unified framework. *J. Chem. Phys.* **149**, 154112 (2018).
36. Pal, A. N. et al. Nonmagnetic single-molecule spin-filter based on quantum interference. *Nat. Commun.* **10**, 5565 (2019).
37. Aragonès, A. C. et al. Measuring the spin-polarization power of a single chiral molecule. *Small* **13**, 1602519 (2017).
38. Vera-Marun, I. J., Ranjan, V. & van Wees, B. J. Nonlinear detection of spin currents in graphene with non-magnetic electrodes. *Nat. Phys.* **8**, 313–316 (2012).
39. Lau, C. S., Mol, J. A., Warner, J. H. & Briggs, G. A. D. Nanoscale control of graphene electrodes. *Phys. Chem. Chem. Phys.* **16**, 20398–20401 (2014).
40. Cornia, A. et al. Magnetic anisotropy of Mn12-acetate nanomagnets from high-field torque magnetometry. *Chem. Phys. Lett.* **322**, 477–482 (2000).
41. Perfetti, M. et al. Determination of magnetic anisotropy in the LnTRENSAL complexes (Ln = Tb, Dy, Er) by torque magnetometry. *Inorg. Chem.* **54**, 3090–3092 (2015).
42. Galván, I. F. et al. OpenMolcas: from source code to insight. *J. Chem. Theory Comput.* **15**, 5925–5964 (2019).
43. Roos, B. O. et al. Main group atoms and dimers studied with a new relativistic ANO basis set. *J. Phys. Chem. A* **108**, 2851–2858 (2004).
44. Roos, B. O., Veryazov, V. & Widmark, P.-O. Relativistic atomic natural orbital type basis sets for the alkaline and alkaline-earth atoms applied to the ground-state potentials for the corresponding dimers. *Theor. Chem. Acc.* **111**, 345–351 (2004).
45. Roos, B. O. et al. New relativistic ANO basis sets for actinide atoms. *Chem. Phys. Lett.* **409**, 295–299 (2005).
46. Roos, B. O. et al. New relativistic ANO basis sets for transition metal atoms. *J. Phys. Chem. A* **109**, 6575–6579 (2005).

Acknowledgements

We thank Kyle Willick and the Quantum Nanofab at the University of Waterloo for help with device fabrication. We thank EPSRC (EP/N017188/1, H.L.A. and L.B.), the European Union (ERC-CoG-773048-MMGNRs—L.B., ERC-CoG-647301-DECRESIM—A.G.-A., ERC-AdG-320969—H.L.A., ERC-StG-851504-ContraVib –COST-15128—N.F.C.), the Royal Society (URF191320—L.B.), and the Spanish MINECO (MDM-2015-0538 and JdIC fellowship—S.C.-S. and A.G.-A.) for financial support.

Author contributions

T.P. fabricated and measured the devices. N.D. developed the measurement setup. J.O.T. synthesized and chemically characterized the compounds in conjunction with H.L.A. J.O.T. performed the transport simulations. S.S. performed the magnetometry. M.-Y.T. and N.F.C. performed ab initio calculations. S.C.-S. and A.G.-A. provided theoretical support. L.B. conceived the experiments. J.O.T. and L.B. treated the data, made all figures, and wrote the first draft. All authors contributed to the final version of the manuscript.

Competing interests

The authors declare no competing interests.

Additional information

Supplementary information The online version contains supplementary material available at <https://doi.org/10.1038/s41467-022-31909-w>.

Correspondence and requests for materials should be addressed to Lapo Bogani.

Peer review information *Nature Communications* thanks the anonymous reviewer(s) for their contribution to the peer review of this work.

Reprints and permission information is available at <http://www.nature.com/reprints>

Publisher's note Springer Nature remains neutral with regard to jurisdictional claims in published maps and institutional affiliations.



Open Access This article is licensed under a Creative Commons Attribution 4.0 International License, which permits use, sharing, adaptation, distribution and reproduction in any medium or format, as long as you give appropriate credit to the original author(s) and the source, provide a link to the Creative Commons license, and indicate if changes were made. The images or other third party material in this article are included in the article's Creative Commons license, unless indicated otherwise in a credit line to the material. If material is not included in the article's Creative Commons license and your intended use is not permitted by statutory regulation or exceeds the permitted use, you will need to obtain permission directly from the copyright holder. To view a copy of this license, visit <http://creativecommons.org/licenses/by/4.0/>.

© The Author(s) 2022